Ordered layered N-doped KTiNbO$_5$/g-C$_3$N$_4$ heterojunction with enhanced visible light photocatalytic activity

Chao Liu[a,b], Huajun Zhu[a], Yisong Zhu[a], Pengyu Dong[c], Haijun Hou[a], Qixiang Xu[a], Xiaowei Chen[a], Xinguo Xi[d,*], Wenhua Hou[b,*]

[a] School of Materials Engineering, Yancheng Institute of Technology, Yancheng, 224051, PR China
[b] Key Laboratory of Mesoscopic Chemistry of MOE, School of Chemistry and Chemical Engineering, Nanjing University, Nanjing, 210023, PR China
[c] Key Laboratory for Advanced Technology in Environmental Protection of Jiangsu Province, Yancheng Institute of Technology, Yancheng, 224051, PR China
[d] School of Chemistry & Chemical Engineering, Yancheng Institute of Technology, Yancheng, 224051, PR China

ARTICLE INFO

ABSTRACT

A facile one-step calcination approach for the synthesis of ordered layered N-doped KTiNbO$_5$/g-C$_3$N$_4$ (NTNO/CN) heterojunction composites was developed. It was found that KTiNbO$_5$ layers were in-situ doped by nitrogen atoms to form N-KTiNbO$_5$ and two-layered g-C$_3$N$_4$ nanosheets were formed within the interlayers of N-KTiNbO$_5$ due to the space-confined effects. The photocatalytic performance of the resulted composites was evaluated by the degradation of rhodamine B (RhB) and bisphenol A (BPA) under visible light irradiation. N-KTiNbO$_5$ coupled with a proper amount of g-C$_3$N$_4$ exhibited an excellent photocatalytic performance due to the synthetic effects of N doping and layered heterojunction, leading to the high efficiency of light harvesting and charge separation. Especially, the in-situ intercalated two-layered g-C$_3$N$_4$ nanosheets can significantly increase the contact area with N-KTiNbO$_5$ layers for efficient charge transfer across the interface, showing a much greater effect on the enhanced photocatalytic activity than those on the pure surface of N-KTiNbO$_5$. It is expected that such a layered heterojunction can greatly speed up the separation and efficient transfer of photogenerated charge carriers. The active species of ·O$_2^-$ played a leading role in the photocatalytic process while h$^+$ contributed to a lesser extent during the photocatalytic degradation of RhB over NTNO/CN-1, as determined by the active species capture experiment and ESR spectra. This work provides a new insight into the preparation of layered heterojunction hybrids with ordered alternative layered structure, and thus opens up the possibility of 'design-and-build' 2D layered heterojunctions for large-scale theoretical exploration and practical applications.

1. Introduction

Photocatalysis has been intensively investigated and recognized as one of the efficient approaches to solve ever-increasing energy shortage and environmental pollution problems [1–3]. Among the reported photocatalysts, KTiNbO$_5$, as a typical layered semiconductor, has been well studied in view of its unique properties such as layered structure, easy modification, appropriate band position, and favorable charge transfer character [4–6]. However, like TiO$_2$, layered KTiNbO$_5$ itself has a relatively low specific surface area and wide bandgap, showing some drawbacks such as its poor response to visible light and high rate of electron-hole recombination [7]. To achieve a high photocatalytic activity, it is necessary to develop a facile approach to prepare KTiNbO$_5$-based photocatalysts with the enhanced visible light response and prolonged life time of charge carriers.

To address the above-mentioned problems of KTiNbO$_5$, our group

has developed some strategies, such as formation of nanosheets, doping of elements, morphology engineering and construction of heterojunction [8–10]. However, the complicated preparation processes and relatively low efficiency limited their application. Among the above strategies, elements doping, especially N doping, will significantly enhance the visible light response and thus improve the visible-light photocatalytic activity, resulting from the creation of doping energy levels [11].

In addition, the construction of heterojunction photocatalysts has been regarded as an efficient way to enhance the photocatalytic activity due to the improved light harvesting and fast charge transfer [12,13]. Particularly, ultrathin g-C$_3$N$_4$ nanosheet, due to its large surface area, suitable electronic band structure, high physicochemical stability and environmentally benign characteristics, has been coupled with other semiconductors to construct heterojunction photocatalysts with enhanced photocatalytic activities [14–16]. However, the overall

---

efficiency of 0D-2D (such as C-doped ZnO/g-C$_3$N$_4$ [17], Cu$_2$O/g-C$_3$N$_4$ [18]) and 1D-2D (such as TiO$_2$/g-C$_3$N$_4$ [19], WO$_3$/g-C$_3$N$_4$ [20]) g-C$_3$N$_4$-based heterojunction photocatalysts was relatively low.

Recently, intriguing surface effects and physical–chemical properties have gradually been uncovered in 2D hetero-layered materials owing to their large surface-to-volume ratio and confined thickness at an atomic scale. Compared with 0D-2D and 1D-2D heterostructures, layered heterojunction (2D-2D heterostructures) greatly increases the contact area for efficient charge transfer across the interface [21,22]. Up to now, 2D-2D heterojunctions with a high photocatalytic activity have been successfully prepared, such as MoS$_2$/g-C$_3$N$_4$ [23], g-C$_3$N$_4$/Bi$_2$WO$_6$ [24], SnNb$_2$O$_6$/g-C$_3$N$_4$ [25], BiOBr/La$_2$Ti$_2$O$_7$ [26], BiOIO$_3$/BiOI [27], and perovskite oxide/g-C$_3$N$_4$ [28,29], MoS$_2$/Bi$_{12}$O$_{17}$Cl$_{12}$ [30]. Especially, Ho et al have prepared artificially coordinate ultrathin metal chalcogenide hetero-layer structure with the controlled thickness and large-scale theoretical exploration [31]. However, the general method for the preparation of the above layered heterojunction composites firstly needs to develop one of the constituent nanosheets as substrate material, and then another kind of nanosheets were grown on their surface. Thus, the practical application of the layered heterojunction photocatalysts are greatly restricted due to the complicated preparation processes, uncontrollable ordered alternative layered structure and difficult large-scale exploration. Up to now, it is still a challenging task to construct ordered layered heterojunctions by a scalable method, and thus to open up the possibility of 'design-and-build' 2D layered heterojunction for large-scale theoretical exploration and practical applications.

In this work, we developed a facile one-step calcination approach to gain ordered layered N-doped KTiNbO$_5$/g-C$_3$N$_4$ composites, in which KTiNbO$_5$ layers were in-situ doped by nitrogen atoms and two-layered g-C$_3$N$_4$ nanosheets were formed within the interlayers of N-KTiNbO$_5$. The structure, morphology, chemical states and visible-light photocatalytic activity in the degradation of RhB and BPA of the resulted samples have been studied and discussed in detail. Moreover, a possible photocatalytic mechanism was proposed based on the multiple experimental results.

2. Experimental section

2.1. Preparation of ordered layered N-doped KTiNbO$_5$/g-C$_3$N$_4$ composites

Layered KTiNbO$_5$ was prepared by heating a stoichiometric mixture of K$_2$CO$_3$, Nb$_2$O$_5$ and TiO$_2$ in molar ratios of 1:1:2 at 1100 °C for 24 h [32]. For comparison, N-doped KTiNbO$_5$ (denoted as N-KTiNbO$_5$) was prepared according to our previous work [33].

To prepare ordered layered N-doped KTiNbO$_5$/g-C$_3$N$_4$ composites, 2.00 g of KTiNbO$_5$ was finely milled with melamine (1.00, 2.00 and 4.00 g), respectively, and then heated at 450 °C for 5 h in a covered crucible. The obtained samples were treated with 0.1 M HNO$_3$ aqueous solution in order to remove residual nitrogen precursors. The resulted samples were denoted as NTNO/CN-x, where x (x = 0.5, 1 and 2) is the mass ratio of melamine to KTiNbO$_5$. The XRD patterns of NTNO/CN-1 before and after proton exchange reaction with 0.1M HNO$_3$ aqueous solution are shown in Fig. S1. The mass of the resulted NTNO/CN-0.5, NTNO/CN-1 and NTNO/CN-2 were 2.22, 2.78 and 3.98 g, respectively. For comparison, 2.00 g of the pure KTiNbO$_5$ was heated at 450 °C for 5 h. The mass of the obtained calcinated KTiNbO$_5$ was 1.98 g. As the mass of KTiNbO$_5$ was almost unchanged after calcination at 450 °C, the mass percentages of g-C$_3$N$_4$ in NTNO/CN-0.5, NTNO/CN-1 and NTNO/CN-2 were calculated to be 9.7%, 28.1% and 49.8%, respectively, by the formula of $(m_c\text{-}2.0\,g)/m_c$ where m_c represents the mass of the resulted NTNO/CN-x composites.

2.2. Fabrication of mixture hybrid of N-KTiNbO$_5$ and g-C$_3$N$_4$

The bulk g-C$_3$N$_4$ was prepared by thermally decomposing melamine

at 550 °C with a ramp rate of 5 °C/min in a covered crucible, and then kept it at 550 °C for 5 h in static air and cooled to room temperature naturally [34]. The obtained yellow powder was washed with 0.1 M HNO$_3$ aqueous solution and distilled water for several times, and then dried at 60 °C overnight.

In order to further study the role of the in-situ intercalated g-C$_3$N$_4$ and surfaced g-C$_3$N$_4$ in the photocatalysis, 2 g of N-doped KTiNbO$_5$ was dispersed in 50 mL of ethanol, and then 0.97 g of g-C$_3$N$_4$ was added. The resulted suspension was treated with ultrasound for 2 h, and finally dried at 60 °C. The resultant mixture was heated at 450 °C for 5 h in a covered crucible. The resulted sample was denoted as CM-NTNO/CN, in which the mass ratio of N-KTiNbO$_5$ to g-C$_3$N$_4$ in CM-NTNO/CN was theoretically equal to that in NTNO/CN-1. For comparison, a certain amount of pure g-C$_3$N$_4$ was also directly mixed with N-KTiNbO$_5$ and then grinded for 30 min. The obtained sample was denoted as M-NTNO/CN, in which the mass ratio of N-KTiNbO$_5$ to g-C$_3$N$_4$ was theoretically equal to that in NTNO/CN-1.

2.3. Characterization techniques

The morphology was investigated by scanning electron microscopy (SEM, JEOL JEM-6300F) and transmission electron microscopy (TEM, JEOL JEM-200CX, operating at an accelerating voltage of 200 kV). For TEM observation, the samples were dispersed in ethanol by ultrasonic treatment and dropped onto carbon-coated copper grids. XRD patterns of the obtained samples were taken on a Philip-X'Pert X-ray diffractometer with a Cu Kα radiation (λ = 1.5418 Å) and Ni filter at a scanning rate of 0.2°/s. UV–vis diffuse reflectance spectra were obtained on a UV–vis spectrophotometer (Shimadzu, UV-3600) using BaSO$_4$ as reference. X-ray photoelectron spectroscopic (XPS) analysis was carried out on an X-ray photoelectron spectrometer (Thermo Fisher Scientific, K-Alpha) equipped with a hemispherical electron analyzer (pass energy of 20 eV) and an Al Kα ($h\nu$ = 1486.6 eV) X-ray source. The binding energies (BE) were referenced to the adventitious C 1s peak (284.6 eV) which was used as an internal standard to take into account charging effects. A combination of Gaussian and Lorentzian functions was used to fit the curves. The Brunauer–Emmett–Teller (BET) specific surface areas were measured by N$_2$ adsorption-desorption isotherms determined at 77 K on a Micromeritics ASAP 2020 surface area and porosity analyzer. Before the measurements, the samples were outgassed at 300 °C for 20 h. Photoluminescence (PL) spectra were recorded on a 48000DSCF luminescence spectrometer at room temperature by using a continuous-wave 325 nm He-Cd laser as the excitation source. The samples were pressed into a thin disk and fixed in a homemade quartz cell. Time-resolved PL (TR-PL) decay spectra were detected by a F900 fluorescence spectrometer with an excitation wavelength of 375 nm.

The electrochemical measurement was carried out in a conventional three-electrode cell on an electrochemical station (Shanghai Chenhua CHI-660D). First, 10 mg catalyst sample was mixed with 20 μL distilled water, 20 μL ethanol and 10 μL nafion under ultrasound. Then the formed homogeneous suspension was spin-coated onto an ITO glass electrode. At last, the electrode was dried naturally for 12 h and then dried at 120 °C for 5 h. The photocurrent was measured in 0.1 M Na$_2$SO$_4$ aqueous solution. A 500 W Xe arc lamp (λ > 420 nm) was served as a light source. The counter and reference electrodes were platinum wire and Ag/AgCl, respectively.

Electron spin resonance (ESR) spectra for hydroxyl (·OH) and superoxide radicals (·O$_2{}^-$) were taken on an ER200-SRC electron spin resonance spectrometer (Bruker, Germany) at 3450 G and 9.818 GHz. Before recording, 10.0 mg sample was dissolved in 0.5 mL deionized water or methanol, and then 30 μL of 5,5-diemthyl-1-pyrroline N-oxide (DMPO) was added with ultrasonic treatment for 5 min, respectively.

2.4. Photocatalytic degradation reaction tests

The visible light photocatalytic activity was evaluated by the degradation of RhB and BPA in aqueous solution. A 300 W Xe lamp with a UV light filter film (to remove radiation with λ < 420 nm) was chosen as the visible light source. The detailed optical and power densities are listed in Table S1. All the photocatalytic degradation experiments were carried out in a beaker with a circulating water system to remove the thermal effect of light. For all degradations, 100 mg of catalyst was firstly suspended in a RhB (4 mg/L) or BPA (2 mg/L) aqueous solution in the dark for 40 min, in order to gain the adsorption-desorption equilibrium. After equilibrium, the resulted suspension was then irradiated under visible light. When the light was turned on, the reaction suspension at intervals of 20 min was sampled and separated by high-speed centrifugation. The concentration was analyzed with a Shimadzu UV-2250 spectrophotometer by recording the maximum absorbance of RhB at 554 nm and that of BPA at 276 nm. The degradation efficiency at time t was determined from the value of C_t/C_0, where C_0 is the initial concentration and C_t is the concentration at time t.

The high performance liquid chromatography (HPLC) (1260 Infinity, Agilent Inc., USA) with an Agilent Eclipse XDB-C18 column (4.6 × 150 mm) was also used to evaluate the photocatalytic removal of BPA. Additionally, 50% acetonitrile and 50% deionized water (containing 0.1% formic acid) were used as the mobile phase at a flow rate of 1.0 mL/min, and the detection wavelength was 273 nm.

The total organic carbon (TOC) was detected with a TOC analyzer (Shimadzu, model TOC-LCPH) to investigate the mineralization degree of the pollutants.

2.5. Active species trapping

In order to detect active species during the photocatalytic reaction, different radical scavengers such as ethylenediaminetetraacetic acid disodium salt (EDTA, 1 mM), *tert*-butyl alcohol (*t*-BuOH, 5 mM) and p-benzoquinone (BZQ, 1 mM) were added to the RhB aqueous solution, respectively. Then, the remaining experimental processes were similar to the above photocatalytic test.

3. Results and discussion

3.1. Morphology

SEM images of the as-prepared KTiNbO₅ in Fig. 1a and Fig. S2a clearly shows a layered structure with the smooth surface. After N-doping, a similar layered morphology is observed for N-KTiNbO₅ (Fig. 1b and Fig. S2b) with a little disorder and the surface of plates became rough. After calcination of KTiNbO₅ with melamine, the resulted NTNO/CN-1 (Fig. 1c and Fig. S2c) also clearly shows a layered structure. However, the surface roughness of NTNO/CN-1 is greatly increased as compared with KTiNbO₅ and N-KTiNbO₅, despite the fact that the overall crystallinity is decreased. The above changes in the morphology of NTNO/CN-1 may be due to the introduction of g-C₃N₄.

As shown in Fig. 1d, TEM image of NTNO/CN-1 displays relatively homogeneous surface and overlapped sheets, indicating that the layered structure is maintained. In addition, some shadow areas are observed on the overlapped sheets, which may be due to the formation of g-C₃N₄. Furthermore, the SEM-EDS mapping images show the presence of C, N and O elements on the surface of KTiNbO₅ (Fig. S3), which also confirms the formation of g-C₃N₄.

From HRTEM images of NTNO/CN-1 (Fig. 1e and f), a layered structure can be clearly observed, while the lattice fringes are obscure and difficult to recognize due to the deposition of amorphous g-C₃N₄, which is confirmed by HRTEM image and the selected area electron diffraction (SAED) pattern of g-C₃N₄ in Fig. 1g. From the enlarged HRTEM image of NTNO/CN-1 (Fig. 1f), the low-resolution interplanar spacing of lattice fringes is about 1.81 nm, which is larger than d_{002}-

spacing of KTiNbO₅ (0.92 nm) [35]. The increased interlayer distance may be arisen from the formation of g-C₃N₄ within the interlayers of KTiNbO₅. The formation mechanism of the in-situ intercalated g-C₃N₄ is mainly due to the fact that the ammonia-based gas released during the pyrolysis of melamine flowed into the interlayer region of KTiNbO₅, and then underwent a confined growth of g-C₃N₄ [36,37]. Obviously, in this approach, layered KTiNbO₅ plays crucial role by providing nucleation sites on the [TiNbO₅]⁻ layers and confining the growing region of g-C₃N₄ during polycondensation process. Meanwhile, the layers of KTiNbO₅ can be in-situ doped by nitrogen atoms to form N-KTiNbO₅ due to the presence of nitrogen-rich precursor melamine, leading to the visible-light response of KTiNbO₅ [38]. The thickness of [TiNbO₅]⁻ layers is 0.680 nm [33]. The theoretical thickness for monolayer g-C₃N₄ nanosheets is 0.325 nm, and d_{100}-spacing of g-C₃N₄ is 0.680 nm [39]. By subtracting the thickness of [TiNbO₅]⁻ layer, the gallery height is estimated to be 1.13 nm, which is higher than the sum of d_{100}-spacing of g-C₃N₄ (0.680 nm) and the thickness of monolayer g-C₃N₄ nanosheets (0.325 nm). By subtracting d_{100}-spacing of g-C₃N₄ and the thickness of monolayer g-C₃N₄ nanosheets, the remaining gallery height is estimated to be ∼ 0.125 nm, attributing to the formed interlayers between [TiNbO₅]⁻ layers and g-C₃N₄ layers, showing only two-layer g-C₃N₄ nanosheets within the interlayers of N-KTiNbO₅.

As shown in Fig. S4, a HRTEM image of NTNO/CN-1 confirms that the formed g-C₃N₄ is also deposited on the surface of N-KTiNbO₅. From the enlarged HRTEM image of NTNO/CN-1 (Fig. S4b), the well-resolved interplanar spacing of lattice fringes is about 0.37 nm, corresponding to the (011) plane based on the crystallographic symmetry of KTiNbO₅. Therefore, a closely contacted interface between g-C₃N₄ and N-KTiNbO₅ is formed, with g-C₃N₄ deposited on the surface and in-situ intercalated into the interlayers of N-KTiNbO₅, respectively, resulting in the formation of ordered layered heterojunction between two components so as to speed up the separation rate of photogenerated charge carriers.

3.2. Powder X-ray diffraction (XRD) analysis and BET surface area

The structure and crystallinity of the resulted samples were identified by XRD. As shown in Fig. 2, in the XRD pattern of g-C₃N₄, the small peak at 2θ = 13.0° (0.68 nm) is indexed to the (100) plane, attributed to the interlayer stacking of g-C₃N₄ [40]. The strong peak at 2θ = 27.7° is indexed to the (002) plane of g-C₃N₄, which can be associated with the stacking of conjugated aromatic system [41]. The XRD pattern of the as-prepared layered KTiNbO₅ matches well with the published data (PDF, #54-1155). After N doping, all characteristic peaks are almost unchanged in N-KTiNbO₅, indicating that the layered structure of KTiNbO₅ is well retained.

After calcination of KTiNbO₅ with different amounts of melamine in a covered crucible, the main characteristic peaks of KTiNbO₅ are maintained in NTNO/CN-x (x = 0.5, 1 and 2), while the intensity of peaks is decreased due to the introduction of g-C₃N₄. It indicates that the introduction of g-C₃N₄ does not influence the crystal structure of KTiNbO₅. Note that the (002) plane of g-C₃N₄ is overlapped with the (200) plane of KTiNbO₅. Thus, the characteristic peak of g-C₃N₄ cannot be observed in the XRD patterns of NTNO/CN-x (x = 0.5, 1 and 2) composites. Moreover, with the amount of g-C₃N₄ increased in NTNO/CN-x, a new reflection peak appears at ∼6.27° for NTNO/CN-1 and NTNO/CN-2, resulting from the ordered layer-by-layer restacking between g-C₃N₄ nanosheets and N-KTiNbO₅ layers [42,43].

Low-angle XRD patterns (Fig. 2b) for NTNO/CN-x (x = 0.5, 1 and 2) samples exhibit three new broad peaks at 2θ = 5.01 (1.76 nm), 6.27 (1.39 nm) and 8.92° (0.99 nm) in comparison with KTiNbO₅, which fully confirmed the formation of ordered layered heterojunction structure between g-C₃N₄ and N-KTiNbO₅. However, the intensity for peak of 2θ = 5.01°, attributing to the interlayer spacing, is firstly increased and then decreased with a maximum intensity for NTNO/CN-1. The increased intensity may be due to the increasing amount of the in-
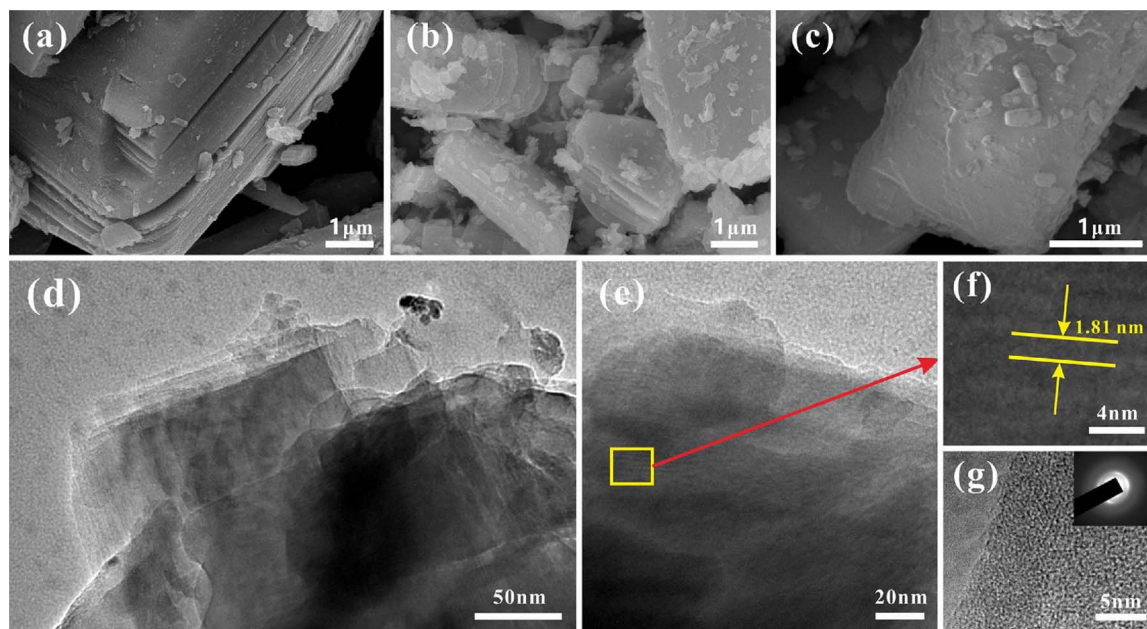
Fig. 1. SEM images of (a) KTiNbO$_5$, (b) N-KTiNbO$_5$ and (c) NTNO/CN-1. TEM (d) and HRTEM images (e, f) of NTNO/CN-1. HRTEM of pure g-C$_3$N$_4$ (g) (inset is the corresponding SAED image).

situ intercalated g-C$_3$N$_4$, while the edge and surface will be covered by g-C$_3$N$_4$ as the mass ratio of g-C$_3$N$_4$ to KTiNbO$_5$ is further increased, leading to the decreased intensity. In particular, there is no change of peak position for all NTNO/CN-*x* samples, indicating that the enlarged interlayer region for the interlayered g-C$_3$N$_4$ is constant, and depends only on the properties of g-C$_3$N$_4$ and N-KTiNbO$_5$. As mentioned above, the thickness of [TiNbO$_5$]$^-$ layer and single-layer g-C$_3$N$_4$ nanosheet is 0.68 nm and 0.325 nm, respectively. Thus, the gallery height is estimated to be 1.08 nm, further indicating that two-layered g-C$_3$N$_4$ nanosheets are formed within the interlayers of N-KTiNbO$_5$ due to the space-confined effect [44], which is in agreement with EM results. The fact that KTiNbO$_5$ and g-C$_3$N$_4$ have analogous layered structures should minimize the lattice mismatch and facilitate the planar growth of g-C$_3$N$_4$ slabs over KTiNbO$_5$ layers [23].

Combined with EM and XRD results, it can be concluded that the formed g-C$_3$N$_4$ are mainly located on the surface and within the interlayers of N-KTiNbO$_5$, respectively and the ordered layered N-KTiNbO$_5$/g-C$_3$N$_4$ heterojunction is thus formed. Especially, ultrathin g-C$_3$N$_4$ nanosheets (two-layers) are formed within the interlayers of N-KTiNbO$_5$ can significantly increases the contact area between N-KTiNbO$_5$ and g-C$_3$N$_4$ for efficient charge transfer across the interface. It is expected that such an ordered layered heterojunction can greatly speed up the separation and efficient transfer of photogenerated charge carriers.

The nitrogen adsorption-desorption isotherms for the resultant samples were shown in Fig. S5. The BET surface area of the pure KTiNbO$_5$ is ~5.6 m^2/g. After combining with g-C$_3$N$_4$ (S_{BET} = 16.7 m^2/g), the BET surface areas were increased to 9.8, 21.5 and 28.3 m^2/g for samples of NTNO/CN-0.5, NTNO/CN-1 and NTNO/CN-2, respectively. It is interesting that the BET surface areas of NTNO/CN-1 and NTNO/CN-2 are larger than that of the pure g-C$_3$N$_4$, which is mainly due to the increased interlayer spacing caused by the intercalated g-C$_3$N$_4$, further confirming the formation of g-C$_3$N$_4$ within the interlayers of N-KTiNbO$_5$.

3.3. UV-visible diffuse reflectance spectra and FT-IR spectra

The optical absorptions of KTiNbO$_5$, N-KTiNbO$_5$, NTNO/CN-1 and g-C$_3$N$_4$ were investigated using UV-visible diffuse reflectance spectra. As shown in Fig. 3a, for pure KTiNbO$_5$, only an absorption band in the UV region can be observed, which is ascribed to the band-to-band transition [45]. After N doping, the absorption in both UV and visible light region is enhanced for the resulted N-KTiNbO$_5$, which is mainly due to the formation of an impurity energy level by N doping.

The sample of NTNO/CN-1 shows a relatively stronger absorption in both UV and visible light region than N-KTiNbO$_5$. Apart from in-situ N doping deduced by ammonia-based gas released during the pyrolysis of melamine, the main reason is due to the introduction of narrow-band-
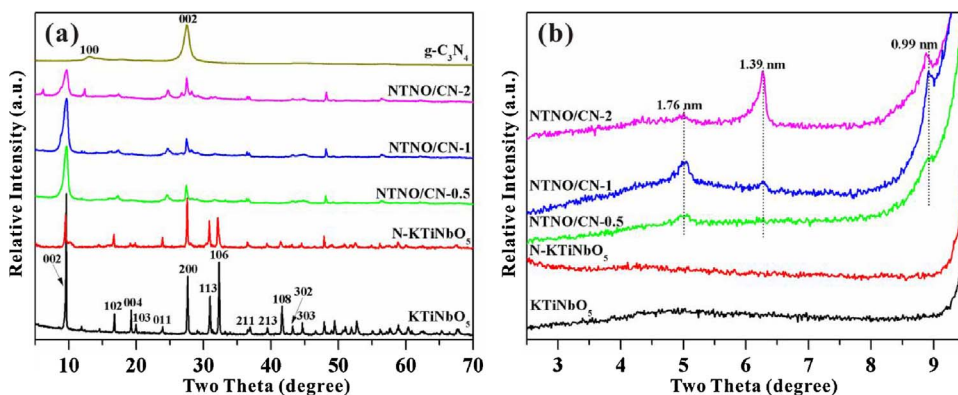

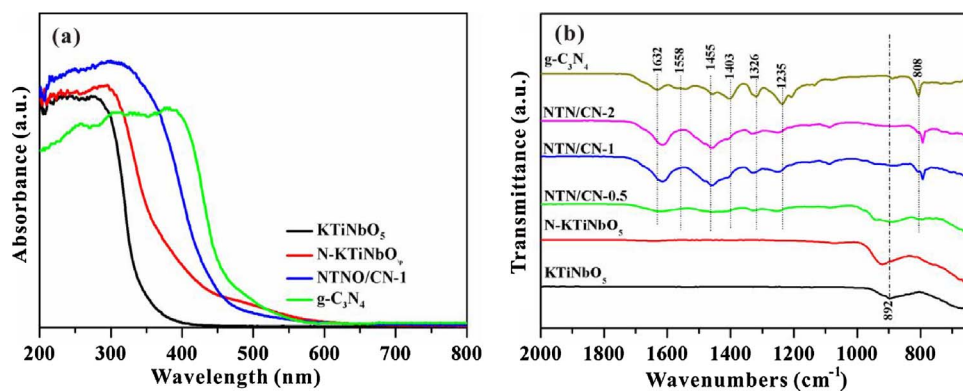**Fig. 2.** XRD patterns (a), and low angle XRD patterns (b) of as-prepared samples.

gap g-C_3N_4. In addition, as shown in Fig. S6, the bandgap energies of $KTiNbO_5$, N-$KTiNbO_5$, g-C_3N_4 and NTNO/CN-1 were estimated to be 3.78, 3.14, 2.69 and 2.70 eV, respectively.

The local structures of the as-prepared photocatalysts were studied using FT-IR. As shown in Fig. 3b, for $KTiNbO_5$ and N-$KTiNbO_5$, the bands at 600–1000 cm^{-1} can be attributed to the octahedral modes of TiO_6 and NbO_6 [4]. As for g-C_3N_4, the absorption band at 808 cm^{-1} is attributed to the characteristic breathing mode of triazine units; the bands at 1235, 1326, 1403, 1455 and 1558 cm^{-1} are related to the typical aromatic C−N stretching vibration; the band at 1632 cm^{-1} is associated with C−N stretching vibration [46–48]. The characteristic absorption bands of g-C_3N_4 are well present for all NTNO/CN-*x* samples, indicating the formation of g-C_3N_4 and thus $KTiNbO_5$/g-C_3N_4 hybrid composite prepared at 450 °C. However, from XRD patterns of g-C_3N_4 prepared at 450 and 550 °C (Fig. S7), it can be clearly seen that pure g-C_3N_4 could not be fully formed at 450 °C, indicating that the preparation temperature of g-C_3N_4 can be greatly decreased in the presence of $KTiNbO_5$. The possible reason for this is that $KTiNbO_5$ shows an analogous layered structure with g-C_3N_4, which is favorable to minimize the lattice mismatch and facilitate the planar growth of g-C_3N_4 slabs over $KTiNbO_5$ layers. Furthermore, compared with g-C_3N_4, it can be clearly seen that the characteristic bands at 1632 and 808 cm^{-1} are shifted to a lower wavenumber for NTNO/CN-*x* composites due to the strong interaction between N-$KTiNbO_5$ and g-C_3N_4 [49]. The conclusion can be further confirmed by XPS analysis.

3.4. XPS analysis

The chemical composition and states of atoms in $KTiNbO_5$, N-$KTiNbO_5$, g-C_3N_4 and NTNO/CN-1 were further determined by XPS. It can be seen from Fig. S8 that the survey spectrum of $KTiNbO_5$ displays C, Ti, Nb and O elements. The carbon peak is attributed to adventitious hydrocarbon from the XPS instrument. The nitrogen peaks appear in the XPS spectra of N-$KTiNbO_5$ and NTNO/CN-1. It should be noted that the intensity of nitrogen peak in NTNO/CN-1 is stronger than that in N-$KTiNbO_5$, as the nitrogen atoms in NTNO/CN-1 can be existed both in the crystal lattice of $KTiNbO_5$ and g-C_3N_4.

As shown in Fig. 4a, two peaks at ~531.5 and ~529.5 eV are observed in the O 1s spectra of $KTiNbO_5$ and N-$KTiNbO_5$, which are attributed to the surface O−H and Ti−O−Ti bond, respectively [50,51]. Compared with $KTiNbO_5$ and N-$KTiNbO_5$, two new peaks at 532.8 and 530.5 eV appear in the O 1s spectrum of NTNO/CN-1, which are ascribed to O − N, and C−O and N−C−O species in the lattice [52]. It is worth noted that there is a shift of O 1s peaks at 531.7 and 529.8 eV for NTNO/CN-1 in comparison with $KTiNbO_5$ and N-$KTiNbO_5$, which indicates that there is a strong interfacial interaction between N-$KTiNbO_5$ layers and g-C_3N_4 nanosheets, resulting from the probable electron transfer and delocalization of two components.

The N 1s binding energy was determined to confirm the chemical state of nitrogen atoms in g-C_3N_4 and NTNO/CN-1. For N 1s spectrum

of g-C_3N_4, three characteristic peaks at 401.0, 399.9 and 398.6 eV are attributed to N−H groups, tertiary nitrogen bonded to carbon atoms (N−(C)$_3$), and sp^2 hybridized aromatic nitrogen bonded to carbon atoms (C=N−C), respectively. These three peaks are quite similar to those in NTNO/CN-1 (400.4, 399.1 and 398.2 eV) with an obvious shift, confirming the formation of g-C_3N_4 [53]. No characteristic peak of doped N in the lattice of $KTiNbO_5$ layers is observed in NTNO/CN-1 due to the low N content and the similar peak position with g-C_3N_4 [10,54]. Additionally, the content of doped N in N-$KTiNbO_5$ is estimated to be 0.93 wt%, while that in NTNO/CN-1 is difficult to obtain due to the overlapped peak position.

Ti 2p and Nb 3d XPS spectra (Fig. 4c and d) were also provided to support the presence of a strong interfacial interaction between g-C_3N_4 nanosheets and N-$KTiNbO_5$ layers. There are the similar Ti 2p and Nb 3d peak values in NTNO/CN-1 and N-$KTiNbO_5$, resulting from the similar chemical states of Ti and Nb atoms between them, which further indicates that $TiNbO_5^-$ layers in NTNO/CN-1 are in-situ doped by N. In the case of NTNO/CN-1, the peak centered at around 458.3 and 464.3 eV can be attributed to the levels of Ti 2p$_{3/2}$ and Ti 2p$_{1/2}$ spin orbital splitting photoelectrons in the Ti^{4+} chemical state, respectively [55]. Compared with pure $KTiNbO_5$, Ti 2p peaks in NTNO/CN-1 and N-$KTiNbO_5$ shift toward the higher binding energies. Similar phenomena are also observed in Nb 3d peaks. These shifts in the binding energies of NTNO/CN-1 further prove the presence of a strong interfacial interaction between g-C_3N_4 nanosheets and N-$KTiNbO_5$ layers.

3.5. Photocatalytic activity

The visible-light photocatalytic performances of the obtained samples were evaluated using RhB aqueous solution as the typical organic contaminant. As shown in Fig. 5a, with the increase of photocatalytic reaction time, a significant decrease of the characteristic absorption band of RhB at 554 nm can be observed, along with a remarkable blue-shift of the maximum absorption. The corresponding reduction in absorbance demonstrates the destruction of the conjugated structure, while the blue-shift of the main absorption band can be ascribed to the step-by-step de-ethylation of RhB [53,56]. The disappearance of these peaks under visible light illumination for 80 min suggests a complete decolorization of the RhB solution.

The stability of NTNO/CN-1 was also studied by recycling the photocatalyst for photodegradation of RhB under visible light irradiation. From Fig. 5b, it is clearly shown that there is no apparent deactivation of the photocatalyst after reuse five times. It demonstrates that the as-prepared NTNO/CN-1 exhibits the excellent photocatalytic stability and activity for the removal of RhB. In addition, XRD patterns and FT-IR spectra in Fig. S9 show no obvious difference between the samples before and after reaction, also indicating a high stability of NTNO/CN-1.

As shown in Fig. 5c, on the basis of a blank test, the self-photolysis of RhB can be neglected under visible light irradiation. For $KTiNbO_5$,
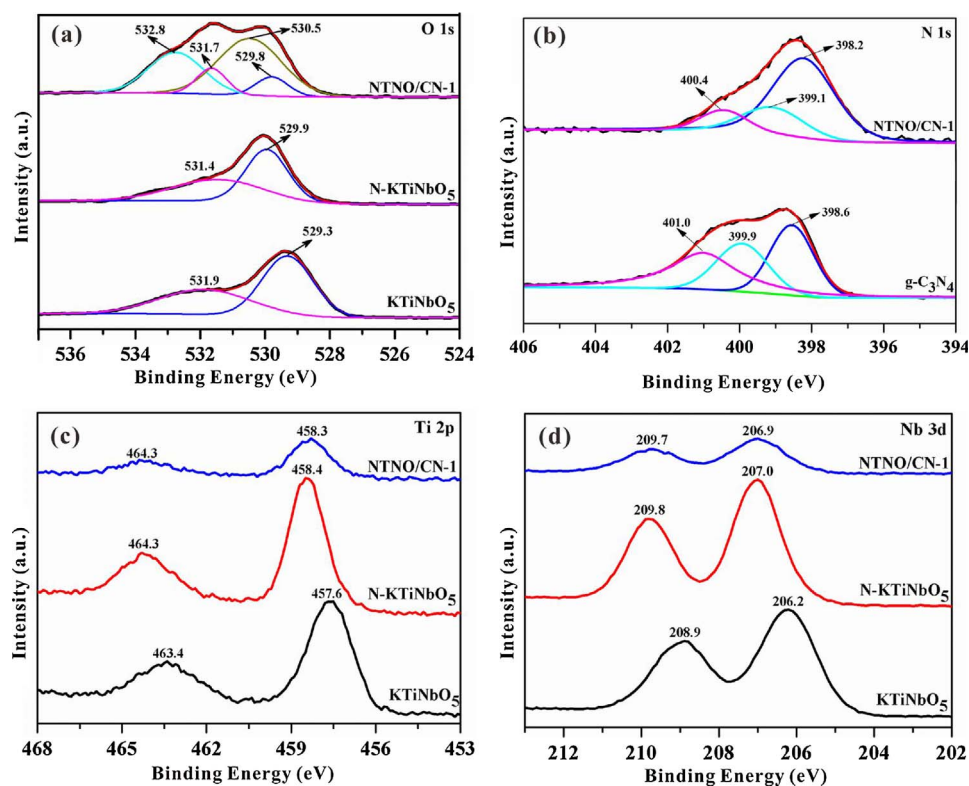
Fig. 4. XPS spectra of (a) O 1s, (b) N 1s, (c) Ti 2p, and (d) Nb 3d of the as-prepared photocatalysts.

the concentration of RhB is only reduced by less than 10% under visible light irradiation within 80 min, due to the self-sensitization oxidation. After N doping, the resulted N-KTiNbO$_5$ shows an enhanced visible-light photocatalytic degradation rate of RhB, attributed to the tuned electronic structure of KTiNbO$_5$ through N-doping and thus the enhancement of the visible-light response of KTiNbO$_5$ [57].

For all NTNO/CN-x composites, the significantly enhanced visible-light photocatalytic activities are observed in comparison with N-KTiNbO$_5$ and g-C$_3$N$_4$. As the loading amount of g-C$_3$N$_4$ is increased, the visible-light photocatalytic activity of NTNO/CN-x series samples first increases with a maximum for NTNO/CN-1, and then decreases. It demonstrates that an appropriate mass ratio of N-KTiNbO$_5$ to g-C$_3$N$_4$ is advantageous for the achievement of excellent activity. The enhanced photocatalytic activity is attributed to N-doping and the formation of ordered layered heterojunction. However, when there is an excess amount of g-C$_3$N$_4$, the thickness of the covered g-C$_3$N$_4$ will increase,
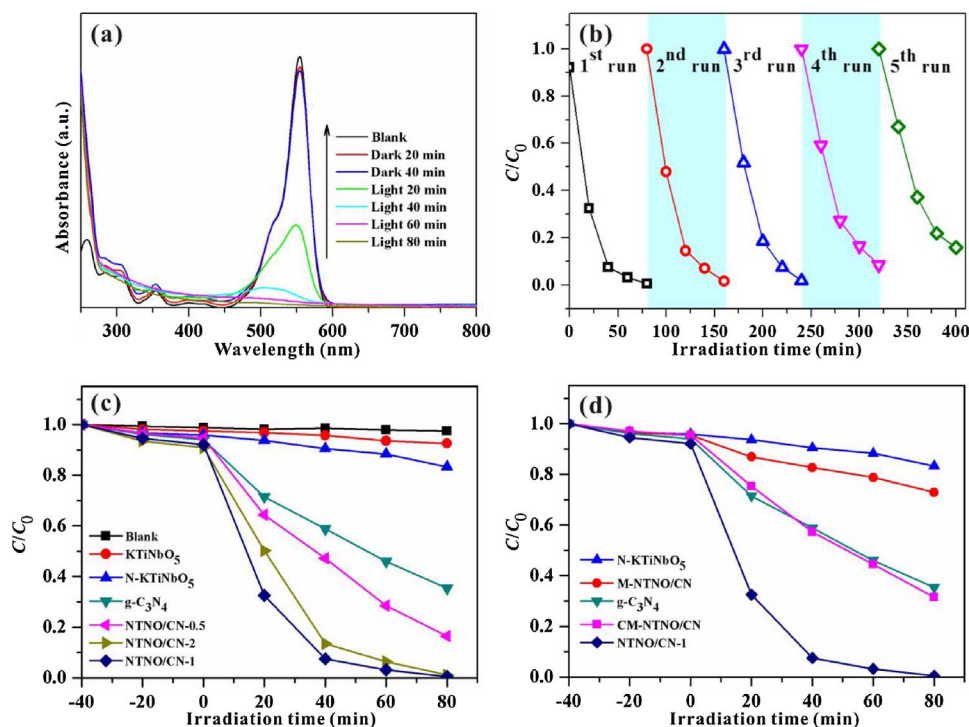

Fig. 5. (a) UV-visible spectral changes, (b) photo-degradation stability, and (c, d) visible light photo-catalytic degradation rate of RhB solution over different samples. (For interpretation of the references to colour in text, the reader is referred to the web version of this article).

and thus the photogenerated electrons of g-C$_3$N$_4$ cannot efficiently migrate to CB of N-KTiNbO$_5$ across the intimate of well-aligned straddling band structures under visible light irradiation, leading to the reduction of photocatalytic activity.

To further determine the different roles of surfaced and in-situ intercalated g-C$_3$N$_4$, the visible-light photocatalytic degradation of RhB solution over different samples was also performed. As shown in Fig. 5d, the photocatalytic activity of the simply mixed sample of M-NTNO/CN is higher than N-KTiNbO$_5$ but lower than pure g-C$_3$N$_4$ due to the lack of efficient interfacial interaction between N-KTiNbO$_5$ and g-C$_3$N$_4$. On the other hand, after calcinating the mixture of N-KTiNbO$_5$ and g-C$_3$N$_4$, g-C$_3$N$_4$ is mainly deposited on the surface of N-KTiNbO$_5$ to form CM-NTNO/CN heterojunction composite, showing the enhanced photocatalytic activity. However, the photocatalytic activity of NTNO/CN-1 is much higher than that of CM-NTNO/CN. Because the separation and transfer of photogenerated charge carriers efficiency of ordered layered N-KTiNbO$_5$/g-C$_3$N$_4$ heterojunction with g-C$_3$N$_4$ both on the surface and within the interlayers of N-KTiNbO$_5$ is higher than that of CM-NTNO/CN with g-C$_3$N$_4$ only deposited on the surface of N-KTiNbO$_5$. It indicates that the in-situ intercalated g-C$_3$N$_4$ plays a key role in the enhanced photocatalytic activity than the surfaced g-C$_3$N$_4$.

The change of TOC with the time can reflect the mineralization degree of RhB during adsorption and visible-light photodegradation [58]. As shown in Fig. 6a, it can be observed that the TOC removal value is increased to ~89.9% after illumination for 80 min in the presence of NTNO/CN-1, indicating a high mineralization degree. Thus, it can be suggested that NTNO/CN-1 can not only degrade RhB but also mineralize it under visible light irradiation, being served as the efficient photocatalyst to remove dye pollutants in water.

To investigate active species photogenerated in the reaction process on NTNO/CN-1 composite, relevant scavengers were added into the RhB solution to see the variation of degradation rate [24,29]. As shown in Fig. 6b, the addition of BZQ (quencher of $\cdot O_2^-$) results in a significantly decreased activity of NTNO/CN-1, indicating that $\cdot O_2^-$ as the main active species plays an important role in the photocatalytic process. The degradation efficiency of NTNO/CN-1 is decreased to 74.7% upon the addition of EDTA (quencher of h$^+$), while the addition of t-BuOH (quencher of $\cdot$OH) shows little effect on the photodegradation of RhB. It indicates that h$^+$ is another main reactive species and $\cdot$OH contributes little during the photocatalytic degradation of RhB in the NTNO/CN-1 system.

To rule out the photosensitization process, BPA was chosen as a colorless organic pollutant model as it was no absorption in the visible light region [59,60]. As shown in Fig. S10, the direct visible-light photolysis of BPA is almost neglectable in the absence of photocatalyst. In comparison with KTiNbO$_5$, N-KTiNbO$_5$ and g-C$_3$N$_4$, NTNO/CN-x composites show a significantly improved visible-light photocatalytic degradation activity of BPA. Moreover, as the amount of g-C$_3$N$_4$ is increased, the photocatalytic activity of NTNO/CN-x series samples first increases and then decreases with a maximum for NTNO/CN-1. Therefore, NTNO/CN-x composites are also efficient photocatalysts to

degrade a colorless organic pollutant.

The detailed photodegradation procedure of NTNO/CN-1 was also investigated by HPLC. As shown in Fig. S11, the peak with a retention time centered at 5.99 min is attributed to BPA. With the increase of irradiation time, this main peak gradually decreases, indicating the gradual destroy of BPA molecular structure. However, the HPLC chromatogram at 40 min exhibits two other peaks at 4.20 and 2.65 min, ascribed to 4-isopropenylphenol and benzoquinone, respectively [61]. As the process proceeds, the peak intensity of intermediates increases. The HPLC chromatogram obtained at 120 min shows no BPA, but only a small amount of 4-isopropenylphenol and benzoquinone, further revealing the successful removal of BPA. Nevertheless, a small amount of intermediates, such as 4-isopropenylphenol and benzoquinone, are difficult to be fully photodegraded in this system.

3.6. Mechanism discussion

Generally, PL technique can be used to evaluate the recombination process of photogenerated electron-hole pairs [34]. The electron-hole recombination rate depends on the emission intensity. A high PL intensity reveals the severe recombination rate of electron-hole pairs. As shown in Fig. 7a, NTNO/CN-1 shows the lowest emission intensity among all samples, indicating that the recombination of photogenerated electron-hole pairs is greatly inhibited in NTNO/CN-1 due to the formation of highly efficient ordered layered heterojunction between N-KTiNbO$_5$ and g-C$_3$N$_4$ nanosheets.

To better depict the recombination process of photogenerated electron-hole pairs in NTNO/CN-1, TR-PL spectra are shown in Fig. 7b. Generally, the longer lifetime is associated with the fast separation of electron-hole pairs, while the shorter lifetime is ascribed to the recombination of electron-hole pairs [47]. The calculated average lifetime values of pure KTiNbO$_5$ N-KTiNbO$_5$, g-C$_3$N$_4$ and N-TNO/CN-1 are 0.79, 1.88, 2.03 and 6.23 ns, respectively. The prolonged lifetime of NTNO/CN-1 may be attributed to the formation of ordered layered heterojunction between N-KTiNbO$_5$ and g-C$_3$N$_4$ nanosheets, which is consequently favorable for the interfacial electron transfer and then the efficiently reduced recombination of photogenerated electrons and holes, leading to the enhanced visible-light photocatalytic activity.

To further investigate the separation and migration of photogenerated electron-hole pairs, the transient photocurrent responses were measured for N-KTiNbO$_5$, g-C$_3$N$_4$ and NTNO/CN-1. The decay of the photocurrent indicates the recombination of holes with electrons, and a constant current is formed when the generation and transfer of electron-hole pairs reaches the equilibrium. As shown in Fig. 8, the photocurrents of N-KTiNbO$_5$ and g-C$_3$N$_4$ are relatively low, while the photocurrent of NTNO/CN-1 is greatly enhanced, demonstrating that the ordered layered heterojunction, in which there is an intimate contact between N-KTiNbO$_5$ layers and g-C$_3$N$_4$ nanosheets, can facilitate the efficient separation of photogenerated electron-hole pairs and accelerate the interfacial charge transfer. The superior photoelectric reproducibility of NTNO/CN-1 will exploit its potential application in the
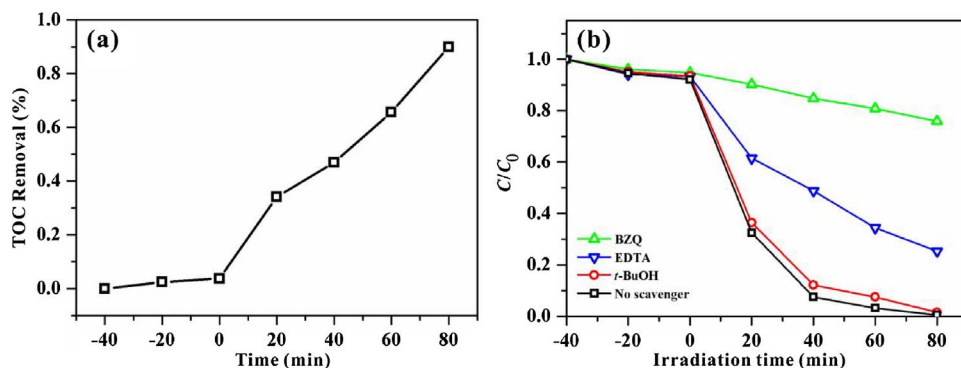

Fig. 6. (a) TOC removal (relative to C_0) of RhB over NTNO/CN-1 under visible light irradiation. (b) effects of different scavengers on the degradation efficiency of RhB over NTNO/CN-1.
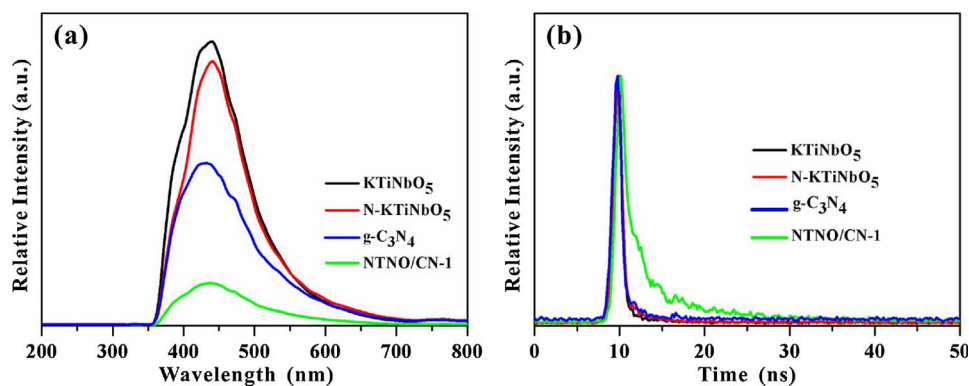
Fig. 7. (a) PL spectra and (b) time-resolved PL decay spectra of KTiNbO$_5$, N-KTiNbO$_5$, g-C$_3$N$_4$ and NTNO/CN-1.
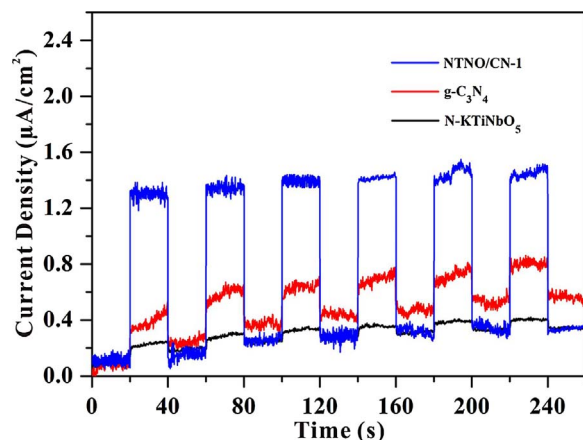

Fig. 8. Transient photocurrent responses under visible light irradiation for different samples.
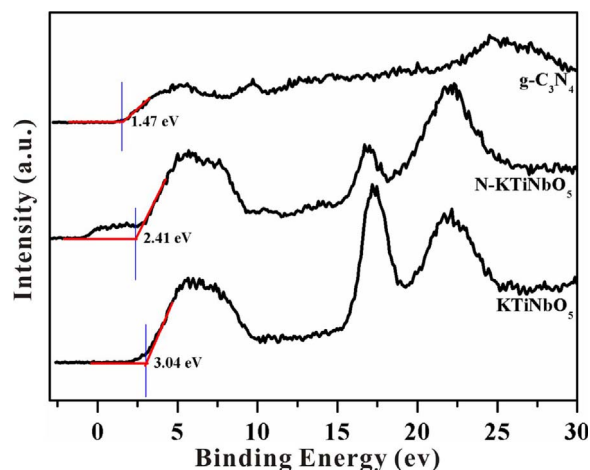

Fig. 10. VB-XPS spectra of KTiNbO$_5$, N-KTiNbO$_5$ and g-C$_3$N$_4$.

fields of solar cell, photodetector, and so on.

The formation of $\cdot$OH and $\cdot O_2^-$ active species during the photocatalytic process was further examined by ESR technique using DMPO as a spin trap to capture $\cdot$OH and $\cdot O_2^-$ under visible light irradiation. Fig. 9 shows that the characteristic peaks of DMPO-$\cdot O_2^-$ can be obviously detected in the methanol dispersion under visible light irradiation while no such signals are observed in dark, indicating that the photogenerated electrons can be transformed into $\cdot O_2^-$ radicals during the photodegradation process. However, the characteristic peaks of DMPO-$\cdot$OH cannot be observed under visible light irradiation. Here, ESR results confirm that only $\cdot O_2^-$ active species are formed during the photocatalytic process and thus give a direct evidence that $\cdot O_2^-$ are mainly responsible for the photodegradation of RhB.

To further study the reasons for highly efficient separation of photogenerated electron-hole pairs, the band energy alignment of the obtained sample was determined by the combination of VB-XPS and DRS. As shown in Fig. 10, the valence bands of the as-prepared KTiNbO$_5$ N-

KTiNbO$_5$ and g-C$_3$N$_4$ are 3.04, 2.41 and 1.47 eV, respectively. Based on the band gaps of KTiNbO$_5$ (3.78 eV) and g-C$_3$N$_4$ (2.69 eV), the valence bands (VB) and conduction bands (CB) of KTiNbO$_5$ and g-C$_3$N$_4$ are calculated to be $+ 3.04/ - 0.74$ eV and $+ 1.47/ - 1.22$ eV, respectively. In other words, the CB and VB potentials of KTiNbO$_5$ and g-C$_3$N$_4$ can be converted to be $+ 2.80/ - 0.98$ V and $+ 1.23/ - 1.46$ V *versus* NHE, respectively, according to the Nernst Equation [62].

According to the above analyses and discussion on charge carrier behavior and band energy levels, the charge transfer and separation processes on NTNO/CN-1 are displayed in Fig. 11. The fact that KTiNbO$_5$ and g-C$_3$N$_4$ have analogous layered structures should minimize the lattice mismatch and facilitate the planar growth of g-C$_3$N$_4$ slabs over KTiNbO$_5$ layers, leading to the formation of ordered layered N-KTiNbO$_5$/g-C$_3$N$_4$ heterojunction. Once irradiated under visible light, both N-KTiNbO$_5$ and g-C$_3$N$_4$ could be excited. The generated electrons in the CB of g-C$_3$N$_4$ will migrate to that of N-KTiNbO$_5$ while holes from N 2p states of N-KTiNbO$_5$ to VB of g-C$_3$N$_4$ across the intimate of well-

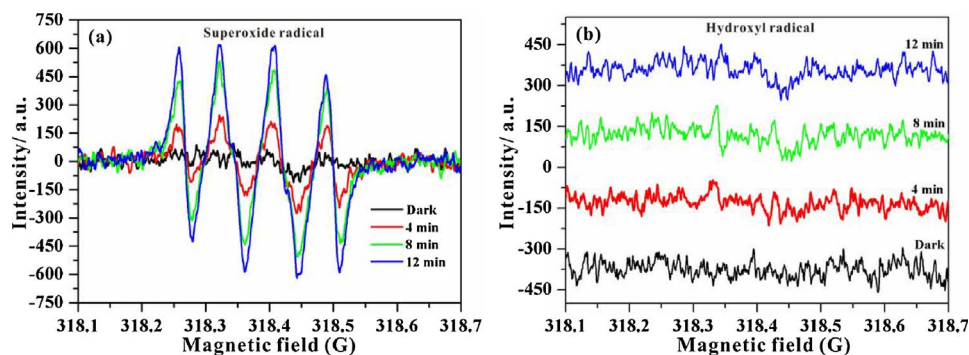**Fig. 9.** ESR spectra of NTNO/CN-1 in aqueous solution before and after visible light irradiation: (a) DMPO-$\cdot O_2^-$ and (b) DMPO-$\cdot$OH.
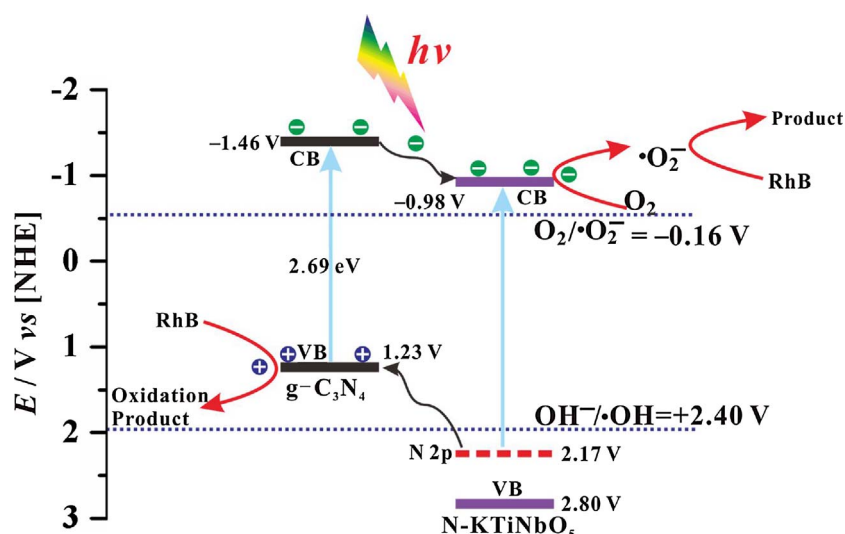
Fig. 11. A schematic illustration of the possible mechanism for charge-transfer and photocatalysis in ordered layered NTNO/CN-1 heterojunction composite under visible-light irradiation.

aligned straddling band structures due to the potential difference. As a result, the photogenerated electrons would be accumulated in CB of N-KTiNbO$_5$ ($E_{CB} = -0.98$ V), which can reduce dissolved oxygen to yield $\cdot O_2^-$ (O$_2$/$\cdot O_2^-$, -0.16 V $vs.$ NHE) [48]. On the other hand, as the VB potential of g-C$_3$N$_4$ ($E_{VB} = +1.23$ V) is much more negative than $\cdot$OH/OH$^-$ ($+2.40$ V $vs.$ NHE) [48], the holes accumulated in VB of g-C$_3$N$_4$ cannot react with OH$^-$ groups or H$_2$O molecules to produce $\cdot$OH radicals. Subsequently, RhB aqueous solution can be directly oxidized by the positive holes in the VB of g-C$_3$N$_4$. The above results are in good agreement with the results of radical species trapping and ESR experiments.

4. Conclusions

In summary, for the first time, we have successfully synthesized ordered layered N-doped KTiNbO$_5$/g-C$_3$N$_4$ heterojunction composites by a facile one-step calcination method, in which KTiNbO$_5$ layers are in-situ doped by nitrogen atoms and two-layered g-C$_3$N$_4$ nanosheets are formed within the interlayers of N-KTiNbO$_5$ due to the space-confined effects. The resulted NTNO/CN composites show an enhanced visible-light photocatalytic activity in the degradation of RhB and BPA, attributing to the synthetic effects of the formation of optimized ordered layered heterojunction and N-doping. Importantly, compared with g-C$_3$N$_4$ on the surface of N-KTiNbO$_5$, the in-situ intercalated g-C$_3$N$_4$ plays a key role in the enhanced photocatalytic activity. A possible photocatalytic mechanism was proposed according to the active species capture experiment and ESR spectra. The active species of $\cdot O_2^-$ play a leading role while h$^+$ contributes to a lesser extent during the photocatalytic degradation of RhB. This work provides a facile approach for the preparation of layered heterojunction hybrids with ordered alternative layered structure, opening up the possibility of 'design-and-build' 2D layered heterojunction for large-scale theoretical exploration and practical applications.

Acknowledgements

Appendix A. Supplementary data

Supplementary material related to this article can be found, in the online version, at doi:https://doi.org/10.1016/j.apcatb.2018.01.074.

References

[1] Y. Zhu, Y. Wang, Q. Ling, Y. Zhu, Appl. Catal. B: Environ. 200 (2017) 222–229.
[2] X. Chen, L. Liu, P.Y. Yu, S.S. Mao, Science 331 (2011) 746–750.
[3] J. Liu, Y. Liu, N. Liu, Y. Han, X. Zhang, H. Huang, Y. Lifshitz, S.-T. Lee, J. Zhong, Z. Kang, Science 347 (2015) 970–974.
[4] C.I. Thomas, M. Karppinen, Inorg. Chem. 56 (2017) 9132–9138.
[5] H.-Y. Lin, Y.-S. Chang, Int. J. Hydrogen Energ. 39 (2014) 3118–3126.
[6] H.-Y. Lin, Y.-S. Chang, Int. J. Hydrogen Energ. 35 (2010) 8463–8471.
[7] Z. Zhai, C.H. Hu, X.Y. Yang, L.H. Zhang, C. Liu, Y.N. Fan, W.H. Hou, J. Mater. Chem. 22 (2012) 19122–19131.
[8] C. Liu, R.R. Han, H.M. Ji, T. Sun, J. Zhao, N.N. Chen, J. Chen, X.F. Guo, W.H. Hou, W.P. Ding, Phys. Chem. Chem. Phys. 18 (2016) 801–810.
[9] Z. Zhai, X.Y. Yang, L. Xu, C.H. Hu, L.H. Zhang, W.H. Hou, Y.N. Fan, Nanoscale 4 (2012) 547–556.
[10] Z. Zhai, Y.C. Huang, L. Xu, X.Y. Yang, C.H. Hu, L.H. Zhang, Y.N. Fan, W.H. Hou, Nano Res. 4 (2011) 635–647.
[11] X.Y. Cai, J.Y. Zhang, M. Fujitsuka, T. Majima, Appl. Catal. B: Environ. 202 (2017) 191–198.
[12] H.L. Wang, L.S. Zhang, Z.G. Chen, J.Q. Hu, S.J. Li, Z.H. Wang, J.S. Liu, X.C. Wang, Chem. Soc. Rev. 43 (2014) 5234–5244.
[13] H.F. Shi, G.Q. Chen, C.L. Zhang, Z.G. Zou, ACS Catal. 4 (2014) 3637–3643.
[14] Z.W. Zhao, Y.J. Sun, F. Dong, Nanoscale 7 (2015) 15–37.
[15] S.W. Cao, J.X. Low, J.G. Yu, M. Jaroniec, Adv. Mater. 27 (2015) 2150–2176.
[16] V.V.-h. Lau, I. Moudrakovski, T. Botari, S. Weinberger, M.B. Mesch, V. Duppel, J. Senker, V. Blum, B.V. Lotsch, Nat. Commun. 7 (2016) 12165.
[17] Y.P. Zhu, M. Li, Y.L. Liu, T.Z. Ren, Z.Y. Yuan, J. Phys. Chem. C 118 (2014) 10963–10971.
[18] J. Chen, S.H. Shen, P.H. Guo, M. Wang, P. Wu, X.X. Wang, L.J. Guo, Appl. Catal. B: Environ. 152 (2014) 335–341.
[19] X. Zhong, M.M. Jin, H.Q. Dong, L. Liu, L. Wang, H.Y. Yu, S. Leng, G.L. Zhuang, X.N. Li, J.G. Wang, J. Solid State Chem. 220 (2014) 54–59.
[20] J. Ding, Q.Q. Liu, Z.Y. Zhang, X. Liu, J.Q. Zhao, S.B. Cheng, B.N. Zong, W.L. Dai, Appl. Catal. B: Environ. 165 (2015) 511–518.
[21] J.X. Xia, M.X. Ji, J. Di, B. Wang, S. Yin, Q. Zhang, M.Q. He, H.M. Li, Appl. Catal. B: Environ. 191 (2016) 235–245.
[22] C.L. Tan, H. Zhang, J. Am. Chem. Soc. 137 (2015) 12162–12174.
[23] Y.D. Hou, A.B. Laursen, J.S. Zhang, G.G. Zhang, Y.S. Zhu, X.C. Wang, S. Dahl, I. Chorkendorff, Angew. Chem. Int. Ed. 52 (2013) 3621–3625.
[24] J.J. Wang, L. Tang, G.M. Zeng, Y.C. Deng, Y.N. Liu, L.L. Wang, Y.Y. Zhou, Z. Guo, J.J. Wang, C. Zhang, Appl. Catal. B: Environ. 209 (2017) 285–294.
[25] Z.Y. Zhang, D.L. Jiang, D. Li, M.Q. He, M. Chen, Appl. Catal. B: Environ. 183 (2016) 113–123.
[26] Y.H. Ao, K.D. Wang, P.F. Wang, C. Wang, J. Hou, Appl. Catal. B: Environ. 194 (2016) 157–168.
[27] F. Dong, T. Xiong, Y.J. Sun, Y.X. Zhang, Y. Zhou, Chem. Commun. 51 (2015) 8249–8252.
[28] S. Thaweesak, M. Lyu, P. Peerakiatkhajohn, T. Butburee, B. Luo, H.J. Chen, L.Z. Wang, Appl. Catal. B: Environ. 202 (2017) 184–190.
[29] D.L. Jiang, T.Y. Wang, Q. Xu, D. Li, S.C. Meng, M. Chen, Appl. Catal. B: Environ. 201 (2017) 617–628.
[30] J. Li, G.M. Zhan, Y. Yu, L.Z. Zhang, Nat. Commun. 7 (2016) 11480.

[31] M.-Q. Yang, Y.-J. Xu, W.H. Lu, K.Y. Zeng, H. Zhu, Q.H. Xu, G.W. Ho, Nat. Commun. 8 (2017) 14224.

[32] L.H. Zhang, C.H. Hu, J.F. Zhang, L.Y. Cheng, Z. Zhai, J. Chen, W.P. Ding, W.H. Hou, Chem. Commun. 49 (2013) 7507–7509.

[33] C. Liu, L. Wu, J. Chen, J.Y. Liang, C.S. Li, H.M. Ji, W.H. Hou, Phys. Chem. Chem. Phys. 16 (2014) 13409–13417.

[34] Z. Wei, F.F. Liang, Y.F. Liu, W.J. Luo, J. Wang, W.Q. Yao, Y.F. Zhu, Appl. Catal. B: Environ. 201 (2017) 600–606.

[35] Z.W. Tong, T. Shichi, K. Takagi, J. Phys. Chem. B 106 (2002) 13306–13310.

[36] W.J. Ong, L.L. Tan, Y.H. Ng, S.T. Yong, S.P. Chai, Chem. Rev. 116 (2016) 7159–7329.

[37] J. Mao, T.Y. Peng, X.H. Zhang, K. Li, L.Q. Ye, L. Zan, Catal. Sci. Technol. 3 (2013) 1253–1260.

[38] R. Asahi, T. Morikawa, H. Irie, T. Ohwaki, Chem. Rev. 114 (2014) 9824–9852.

[39] J. Xu, L.W. Zhang, R. Shi, Y.F. Zhu, J. Mater. Chem. A 1 (2013) 14766–14772.

[40] Z. Wan, G.K. Zhang, X.Y. Wu, S. Yin, Appl. Catal. B: Environ. 207 (2017) 17–26.

[41] X. Xin, J.Y. Lang, T.T. Wang, Y.G. Su, Y.X. Zhao, X.J. Wang, Appl. Catal. B: Environ. 181 (2016) 197–209.

[42] J.L. Gunjakar, T.W. Kim, H.N. Kim, I.Y. Kim, S.-J. Hwang, J. Am. Chem. Soc. 133 (2011) 14998–15007.

[43] L. Li, R.Z. Ma, Y. Ebina, K. Fukuda, K. Takada, T. Sasaki, J. Am. Chem. Soc. 129 (2007) 8000–8007.

[44] X. Zhang, R.F. Zhao, Q.H. Wu, W.L. Li, C. Shen, L.B. Ni, H. Yan, G.W. Diao, M. Chen, ACS Nano 11 (2017) 8429–8436.

[45] L. Liu, J.Y. Liang, R.R. Han, Y.Z. Wang, J. Zhao, Q.J. Huang, J. Chen, W.H. Hou, Phys. Chem. Chem. Phys. 17 (2015) 15165–15172.

[46] G.Q. Tan, L.N. She, T. Liu, C. Xu, H.J. Ren, A. Xia, Appl. Catal. B: Environ. 207 (2017) 120–133.

[47] Z. Lu, L. Zeng, W.L. Song, Z.Y. Qin, D.W. Zeng, C.S. Xie, Appl. Catal. B: Environ. 202 (2017) 489–499.

[48] Y. Li, K.L. Lv, W.K. Ho, F. Dong, X.F. Wu, Y. Xia, Appl. Catal. B: Environ. 202 (2017) 611–619.

[49] Z.Y. Zhang, J.D. Huang, M.Y. Zhang, Q. Yuan, B. Dong, Appl. Catal. B: Environ. 163 (2015) 298–305.

[50] J.C. Huo, Y.J. Hu, H. Jiang, C.Z. Li, Nanoscale 6 (2014) 9078–9084.

[51] K. Li, S.M. Gao, Q.Y. Wang, H. Xu, Z.Y. Wang, B. Huang, Y. Dai, J. Lu, ACS Appl. Mater. Inter. 7 (2015) 9023–9030.

[52] J. Fu, B. Zhu, C. Jiang, B. Cheng, W. You, J. Yu, Small 13 (2017) 1603938.

[53] C. Liu, Q.S. Wu, M.W. Ji, H.J. Zhu, H.J. Hou, Q.H. Yang, C.F. Jiang, J.J. Wang, L. Tian, J. Chen, W.H. Hou, J. Alloy. Compd. 723 (2017) 1121–1131.

[54] C. Liu, T. Sun, L. Wu, J.Y. Liang, Q.J. Huang, J. Chen, W.H. Hou, Appl. Catal. B: Environ. 170–171 (2015) 17–24.

[55] L.D. Li, J.Q. Yan, T. Wang, Z.J. Zhao, J. Zhang, J.L. Gong, N.J. Guan, Nat. Commun. 6 (2015) 5881.

[56] C.C. Chen, W. Zhao, J.Y. Li, J.C. Zhao, H. Hidaka, N. Serpone, Environ. Sci. Technol. 36 (2002) 3604–3611.

[57] X.B. Chen, C. Burda, J. Am. Chem. Soc. 130 (2008) 5018–5019.

[58] Y. Mi, L.Y. Wen, Z.J. Wang, D.W. Cao, Y.G. Fang, Y. Lei, Appl. Catal. B: Environ. 176 (2015) 331–337.

[59] G. Žerjav, M.S. Arshad, P. Djinović, J. Zavašnik, A. Pintar, Appl. Catal. B: Environ. 209 (2017) 273–284.

[60] H.T. Tian, J.W. Li, M. Ge, Y.P. Zhao, L. Liu, Catal. Sci. Technol. 2 (2012) 2351–2355.

[61] L. Yang, Z. Li, H. Jiang, W. Jiang, R. Su, S. Luo, Y. Luo, Appl. Catal. B: Environ. 183 (2016) 75–85.

[62] X. Yang, F. Qian, Y. Wang, M. Li, J. Lu, Y. Li, M. Bao, Appl. Catal. B: Environ. 200 (2017) 283–296.